

Visualization of Acoustic Power Flow in Suspended Thin-film Lithium Niobate Phononic Devices

Daehun Lee¹, Shawn Meyer¹, Songbin Gong³, Ruochen Lu^{*2}, Keji Lai^{*1}

¹Department of Physics, University of Texas at Austin, Austin TX 78712, USA

²Department of Electrical and Computer Engineering, University of Texas at Austin, Austin TX 78712, USA

³Department of Electrical and Computer Engineering, University of Illinois at Urbana-Champaign, Urbana IL, 61801, USA

* E-mails: ruochen@utexas.edu, kejilai@physics.utexas.edu

Abstract

We report direct visualization of gigahertz-frequency acoustic waves in lithium niobate phononic circuits. Primary propagation parameters, such as the power flow angle (PFA) and propagation loss (PL), are measured by transmission-mode microwave impedance microscopy (TMIM). Using fast Fourier transform, we can separately analyze forward and backward propagating waves and quantitatively evaluate the propagation loss. Our work provides insightful information on the propagation, diffraction, and attenuation in piezoelectric thin films, which is highly desirable for designing and optimizing phononic devices for microwave signal processing.

Acoustic-wave devices have been the primary radio frequency (RF) mobile front-end filtering solution in the telecommunication industry [1]. Their commercial success is mostly enabled by shorter wavelength and lower damping of the acoustic wave than the electromagnetic counterpart, resulting in compact signal processing elements with low loss and good frequency selectivity [2]. More recently, as 5G communication and beyond moves toward higher frequencies (> 3 GHz) and wider bandwidths ($> 10\%$) [3], it is not trivial for conventional surface acoustic wave (SAW) [4] and bulk acoustic wave (BAW) [5] platforms to meet the new specifications, as their performance is fundamentally limited by the moderate electromechanical coupling (K^2) and quality factor (Q) at higher frequencies [6]. New acoustic platforms with better frequency scalability and simultaneously high K^2 and Q are thus highly sought after.

In the past decade, Lamb-wave devices in lithium niobate (LiNbO_3) single-crystal thin films have been identified as promising candidates for GHz wideband acoustic signal processing [7]. Thanks to the advance of thin-film transfer technology [8], various acoustic elements have been implemented in suspended LiNbO_3 as mm-wave resonators [9], filters [10, 11], delay lines [12], and amplifiers [13]. Despite the enhanced performance promised by the new platform, it is more challenging to design and optimize GHz acoustic devices in suspended thin-film LiNbO_3 than in conventional piezoelectric platforms. First of all, acoustic waves in thin-film LiNbO_3 are highly anisotropic, causing deviation in direction between phase velocity (v_{ph}) and group velocity (v_{g}), i.e., slanted power flow described by a non-zero power flow angle (PFA) [14]. Without considering PFA, resonant devices with low Q and propagation devices with energy launching off the receiving transducers are inevitable. Secondly, the propagation loss (PL), diffraction, and reflection of GHz acoustic waves in thin-film LiNbO_3 are understudied. Optimizing device performance, e.g., minimizing loss, is thus difficult. Thirdly, the highly piezoelectric substrates

tend to generate spurious modes, i.e., unwanted acoustic vibration near the main tone, via electrical routing and parasitics. It is difficult to identify the origin of such effects merely from electrical measurement. Last but not least, the characterization of acoustic components is limited to terminal-to-terminal electrical response. Researchers have to mostly rely on numerical modeling to understand the GHz acoustic vibration, with little experimental validation on the actual displacement at the nanoscale.

One effective approach for designing LiNbO₃ phononic devices is to directly visualize the acoustic vibration. If available, such measurement would facilitate performance optimization in conventional functions and enable novel applications, e.g., capturing energy leakage in acoustic resonators or mode conversion in phononic circuits. It is also applicable to emerging applications such as topological phononic crystals and acoustic metamaterials. To achieve this goal, many attempts, including optical reflectometry [15, 16] and interferometry [17, 18], stroboscopic X-ray imaging [19, 20], and scanning electron microscopy [21, 22], among others, have been made to probe the acoustic displacement fields. However, none of these techniques can simultaneously achieve sub-100 nm spatial resolution and > 1 GHz operation frequency, which are crucial for technologically relevant devices. A new method that is capable of investigating the nanoscale GHz acoustic phenomena is therefore highly desirable for designing and optimizing advanced phononic circuits.

In this work, we report the visualization of 1 GHz fundamental symmetric mode (S_0 mode) in suspended thin-film LiNbO₃ by transmission-mode microwave impedance microscopy (TMIM) [23-25]. The power flow angle (PFA) is directly measured from the TMIM images and compared to the finite-element simulation. Using fast Fourier transform (FFT), the forward and backward propagation waves are quantitatively analyzed and the propagation loss calculated. Our work

provides insightful information on energy flow inside acoustic structures and suggests a new approach to characterize phononic devices.

The suspended phononic devices in this work were fabricated on 800 nm X-cut LiNbO₃ thin film transferred onto Si carrier chips (NGK Insulators, Ltd). The sputtered electrodes (135 nm thick) were defined by e-beam lithography. A SiO₂ layer (2 μm in thickness) was deposited using plasma-enhanced chemical vapor deposition (PECVD) as the hard mask and patterned by fluorine-based reactive ion etching (RIE). The release windows in the LiNbO₃ film were subsequently etched using chlorine-based inductively coupled plasma reactive ion etching (ICP-RIE). The remaining SiO₂ was removed by low-power ICP. The devices were then released by isotropic XeF₂-based silicon etching. As shown in Fig. 1a, the acoustic waveguide (width $w = 150 \mu\text{m}$ and length $L = 700 \mu\text{m}$) with 4 ports of single-phase unidirectional transducers (SPUDTs) is oriented 15° away from the y axis. [26]

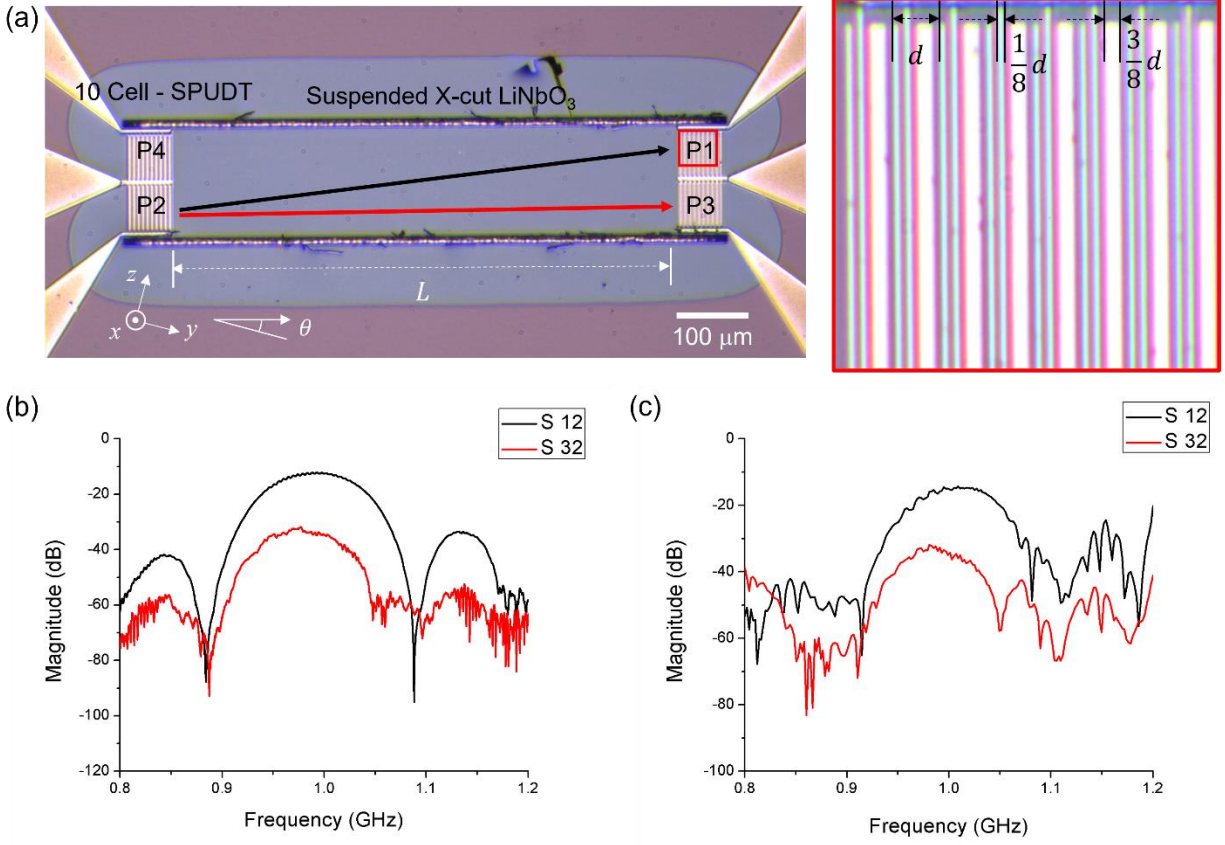


FIG. 1. (a) Optical image of the suspended X-cut LiNbO₃ waveguide and four ports of 10-cell single-phase unidirectional transducers (SPUDTs). The waveguide direction is tilted by $\theta = 15^\circ$ from the y-axis. The red and black arrows indicate the power transmission from Port 2 to Port 3 and Port 1, respectively. The inset on the right shows a magnified image of the boxed region. One unit cell of the SPUDT consists of three fingers, one ($d/8$ in width, where d is the wavelength) connected to the signal electrode and two ($d/8$, and $3d/8$ in widths) connected to the ground electrode. (b) S_{12} and S_{32} spectra of the device measured by a VNA, showing the acoustic passband at $f = 1.00$ GHz. Note that S_{12} is significantly higher than S_{32} in the passband. (c) Finite-element simulation results of S_{12} and S_{32} spectral.

Electrical characterization of the LiNbO₃ waveguide test structure was first carried out with a vector network analyzer (VNA). Here the acoustic wave is launched from Port 2 and received at Ports 1 and 3. The measured transmission coefficients S_{12} and S_{32} are plotted in Fig. 1b. Inside the S_0 passband centered at $f = 1.00$ GHz, it is clear that S_{12} is significantly higher than S_{32} by ~ 20 dB, indicative of the slanted power flow. In order to understand the power transmission, we also modeled the SPUDTs and acoustic waveguide by finite-element analysis (FEA). The simulated S_{12} and S_{32} in Fig. 1c are in good agreement with the measured results in Fig. 1b.

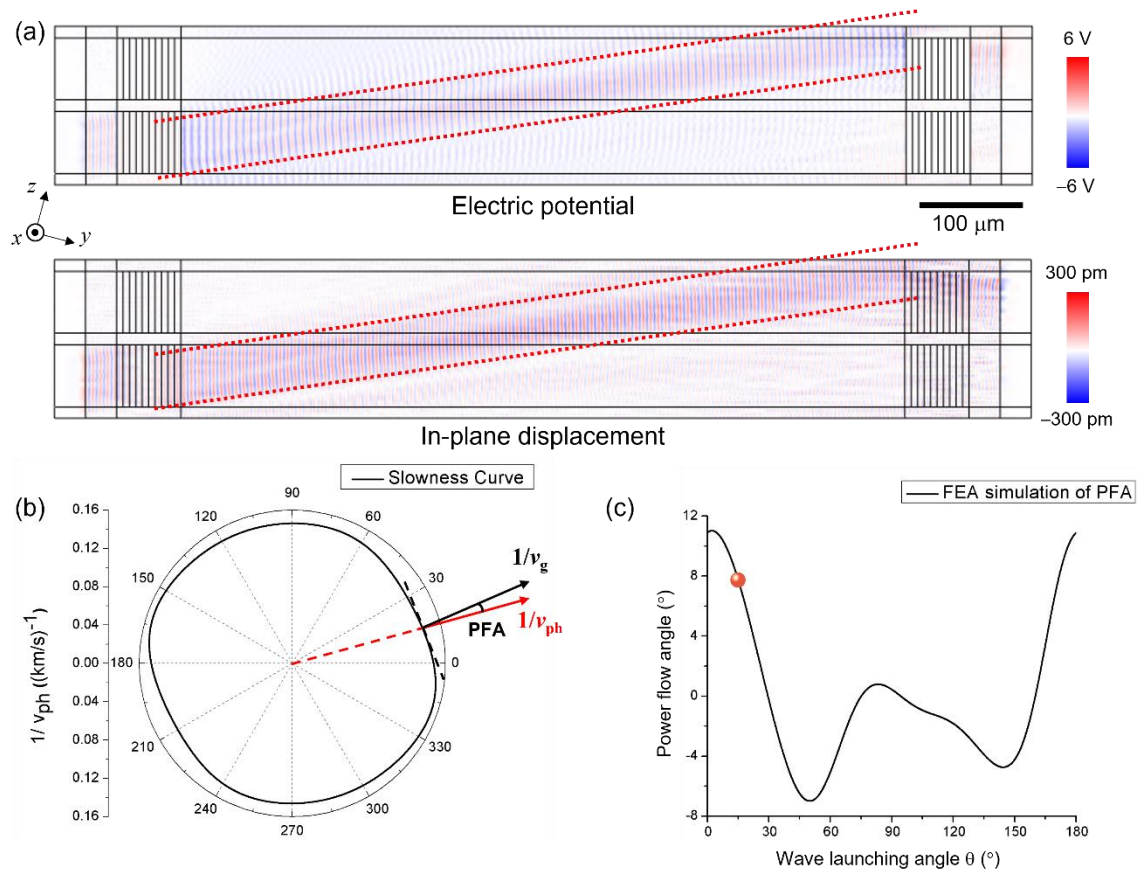


FIG. 2. (a) FEA of electric potential (upper panel) and in-plane displacement along the waveguide direction (lower panel) of the LiNbO₃ thin-film waveguide device under 3 dBm excitation power. (b) FEA simulated slowness curve of S_0 (thick black curve) in unmetallized LiNbO₃ thin film along different angles to +y-axis (outer circle). The acoustic wave in this work is launched at $\theta = 15^\circ$ (red dashed line and arrow). The direction of the group velocity is normal to the slowness curve (black arrow). The angle between the two vectors defines the power flow angle (PFA). (c) Simulated PFA as a function of the wave launching angle. The orange dot denotes the PFA at $\theta = 15^\circ$.

The simulated surface potential and total in-plane displacement field on the LiNbO₃ device are shown in Fig. 2a. The results clearly demonstrate that the slanted acoustic wave propagation, which stems from the difference in direction between phase velocity (v_{ph}) and group velocity (v_g) [14]. Fig. 2b plots the S_0 slowness curve, i.e., $1/v_{ph}$ along launching angles from 0 to 2. The PFA is then determined by the angle between the phase velocity (along the wave launching by SPUDT) and the group velocity (along the normal line of the slowness curve). Fig. 2c shows the simulated

PFA as a function of the wave launching angle. At $\theta = 15^\circ$, the simulation indicates that PFA is $\sim 7.7^\circ$, which is consistent with previous reports [27, 28].

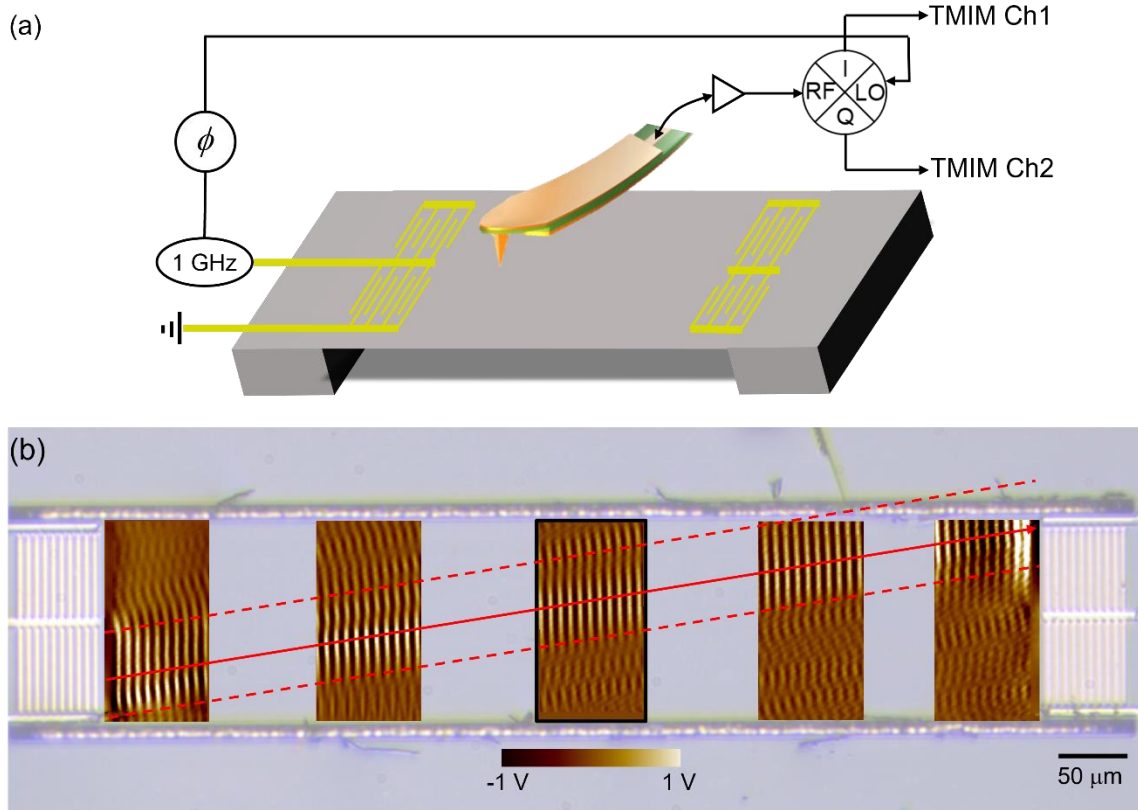


FIG. 3. **(a)** Schematic of the TMIM imaging on a suspended waveguide. **(b)** TMIM images overlaid on top of an optical picture of the device. The red arrow and dashed lines denote the propagation direction and approximate boundaries of the acoustic wave.

Visualization of the Lamb wave on thin-film LiNbO_3 waveguide was carried out by TMIM, an atomic-force-microscopy (AFM)-based technique with sub-100nm spatial resolution [23-25]. Fig. 3a shows the schematic of the experiment, where the acoustic wave is launched by the emitter SPUDT and the induced piezoelectric potential at 1.00 GHz is detected by the tip. The signal is then amplified and demodulated by an in-phase/quadrature (I/Q) mixer, which converts time-varying acoustic signals to time-independent impedance images. The complex-valued TMIM signal $V_{\text{Ch1}} + i * V_{\text{Ch2}}$ thus provides a phase-sensitive measurement on the local displacement field of the Lamb wave. Fig. 3b shows images from one of the two TMIM channels taken at various

locations on the device. The prominent Lamb wave launched from Port 2 is planewave-like with wavefront parallel to the emitter SPUDT. The acoustic power flow, on the other hand, clearly deviates from the wave launching direction. By tracking the maximum intensity in the TMIM images along the LiNbO₃ waveguide (red arrow), we can estimate a PFA $\sim 8^\circ$ for this device, which matches well with the simulated result above. It should be noted that, in addition to the primary wave bounded by the dashed lines in Fig. 3b, scattered waves due to waveguide boundaries and interference pattern due to multiple reflections are observed in the TMIM images. These imperfections are sample-dependent and difficult to be simulated by FEA. Careful analysis of these secondary features could help optimize device performance in future studies.

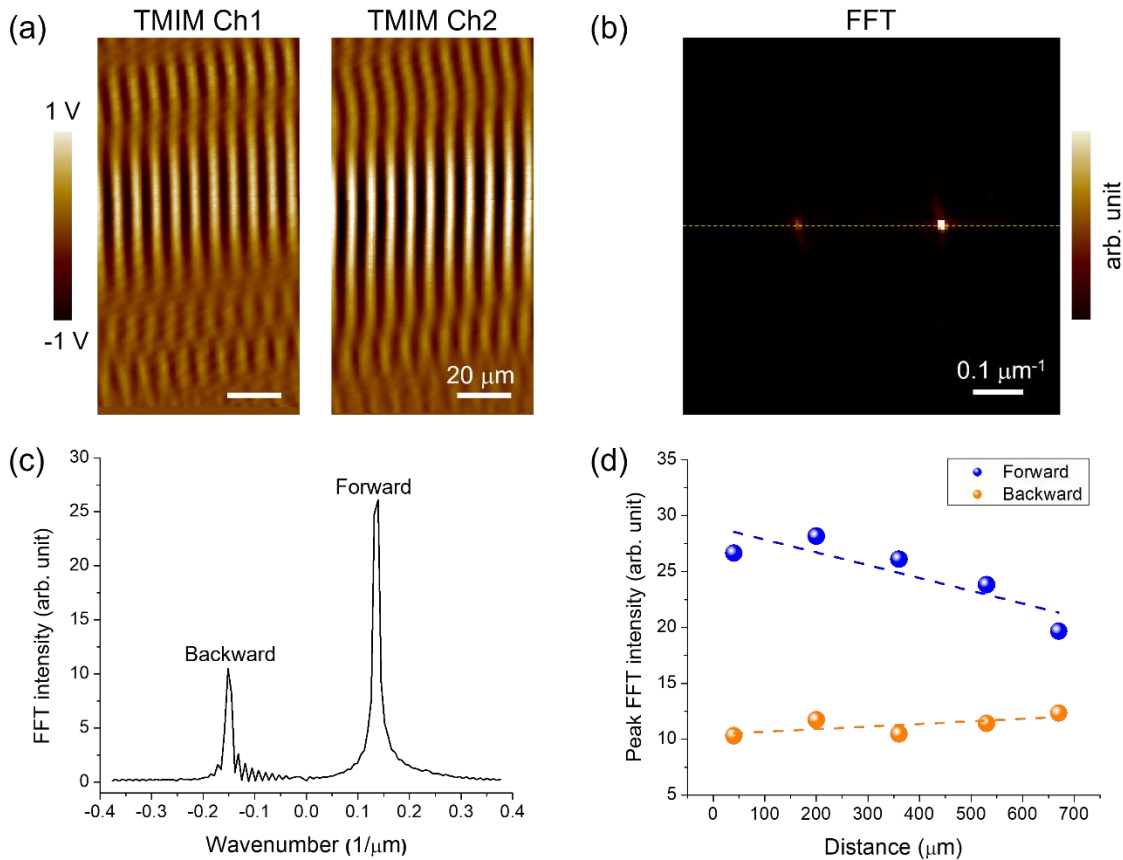


FIG. 4. (a) Simultaneously demodulated TMIM Ch1 and Ch2 images near the center of the testbed device. (b) FFT amplitude map of the TMIM data in a. (c) Line profile across the yellow dashed line in b. (d) Peak FFT intensity of TMIM results as a function of distance from the wave launching port. The blue and orange dots represent the forward and backward propagation, respectively. Dashed lines are linear fits to the data.

In addition to imaging acoustic waves, the TMIM also allows us to perform quantitative analysis of the power flow in LiNbO₃ waveguides. Specifically, the momentum-space information can be obtained by taking FFT [25] of the combined signal $V_{\text{Ch1}} + i * V_{\text{Ch2}}$. Fig. 4a displays the TMIM images from the two orthogonal channels at the center of the suspended device (outlined in black in Fig. 3b). The corresponding FFT amplitude map near zero wavenumber is shown in Fig. 4b, where two high-intensity spots are clearly seen along the waveguide direction. In Fig. 4c, we plot the line profile across the dashed line in Fig. 4b. The peaks on the left and right correspond to the right-moving and left-moving Lamb waves, respectively. Since the FFT amplitude is directly proportional to the magnitude of the waves, we can estimate that, at this location, the power of the forward-propagating wave is ~ 7 times higher than that of the backward one from the ratio between these two intensity peaks. By plotting the peak height as a function of the position (Fig. 4d), we can calculate PLs of ~ 4.0 dB/mm for the forward wave and ~ 1.8 dB/mm for the backward wave, which are comparable to that reported in suspended LiNbO₃ thin films [29]. The difference in PL between wave propagating in opposite directions requires further investigations. Nevertheless, we emphasize that such phase-sensitive information is not readily available from other spatially resolved methods that mainly probe the surface oscillation amplitude. Given its advantages of high operation frequency, superior spatial resolution, and phase-sensitive detection of piezoelectric potential, the TMIM is expected to play a major role in future studies of acousto-electronic systems.

To summarize, we report the fabrication of suspended LiNbO₃ acoustic waveguides and the visualization of slanted power flow of acoustic waves on such phononic devices. Combining finite-element modeling and transmission-mode microwave microscopy, we are able to directly measure the power flow angle, which is in good agreement with the calculated value. FFT analysis of the two orthogonal microwave images yields crucial information on the forward-propagating

and reflected waves, from which the propagation loss can be evaluated. Our work demonstrates the exquisite sensitivity and high resolution of the TMIM technique in characterizing phononic circuits, which may find widespread applications in electromechanics, optomechanics, and quantum science and engineering.

ACKNOWLEDGMENTS

The TMIM work was supported by NSF Division of Materials Research Grant DMR-2004536 and Welch Foundation Grant F-1814. The phononic device fabrication work was supported by DARPA Microsystems Technology Office (MTO) Near Zero Power RF and Sensor Operations (N-ZERO) project programs.

DATA AVAILABILITY

The data that support the findings of this study are available from the corresponding author upon reasonable request.

References:

- [1] R. Ruby, A Snapshot in Time: The Future in Filters for Cell Phones. *IEEE Microwave Magazine* **16**, 46-59 (2015).
- [2] T. Bauer, C. Eggs, K. Wagner, and P. Hagn, A Bright Outlook for Acoustic Filtering: A New Generation of Very Low-Profile SAW, TC SAW, and BAW Devices for Module Integration. *IEEE Microwave Magazine* **16**, 73-81 (2015).
- [3] A. Ghosh, A. Maeder, M. Baker, and D. Chandramouli, 5G Evolution: A View on 5G Cellular Technology Beyond 3GPP Release 15. *IEEE Access* **7**, 127639-127651 (2019).
- [4] K. Y. Hashimoto, *Surface Acoustic Wave Devices in Telecommunications: Modeling and simulation*. Springer-Verlag, Berlin (2000).
- [5] K. Y. Hashimoto, *RF bulk acoustic filters for communications*. Artech House, Boston (2009).
- [6] *IEEE Standard on Piezoelectricity*, ANSI/IEEE Std 176-1987, 1-1988 (1988).
- [7] S. Gong, R. Lu, Y. Yang, L. Gao, and A. E. Hassanien, Microwave Acoustic Devices: Recent Advances and Outlook. *IEEE Journal of Microwaves* **1**, 601-609 (2021).
- [8] M. Pijolat, A. Reinhardt, E. Defay, C. Deguet, D. Mercier, M. Aid, J.S. Moulet, B. Ghyselen, D. Gachon, and S. Ballandras, Large Qxf product for HBAR using Smart Cut™ transfer of LiNbO₃ thin layers onto LiNbO₃ substrate. *2008 IEEE Ultrasonics Symposium*, 201-204 (2008).
- [9] Y. Yang, R. Lu, L. Gao, and S. Gong, 10–60-GHz Electromechanical Resonators Using Thin-Film Lithium Niobate. *IEEE Transactions on Microwave Theory and Techniques* **68**, 5211-5220 (2020).
- [10] Y. Yao, B. Liu, H. Zhang, H. Liu, and J. Liu, Design of thin-film lithium niobate structure for integrated filtering and sensing applications. *Result in Physics* **17**, 103082 (2020).
- [11] Y. Yang, R. Lu, L. Gao, and S. Gong, 4.5 GHz Lithium Niobate MEMS Filters With 10% Fractional Bandwidth for 5G Front-Ends. *J. Microelectromechanical Systems* **28**, 575-577 (2019).
- [12] C. J. Sarabalis, Y. D. Dahmani, A. Y. Cleland, and A. H. Safavi-Naeini, S-band delay lines in suspended lithium niobate. *J. Appl. Phys.* **127**, 054501 (2020).
- [13] Z. Chen, Q. Xu, K. Zhang, W. H. Wong, D. L. Zhang, E. Y. B. Pun, and C. Wang, Efficient erbium-doped thin-film lithium niobate waveguide amplifiers. *Optics Letter* **46**, 5 (2021).
- [14] D. Royer and E. Dieulesaint, *Elastic Waves in Solids I*, Springer-Verlag Berlin 1996.
- [15] A. Mahjoubfar, K. Goda, A. Ayazi, A. Fard, S. H. Kim, and B. Jalali, High-speed nanometer-resolved imaging vibrometer and velocimeter. *Appl. Phys. Lett.* **98**, 101107 (2011).
- [16] Y. Xu, W. Fu, C.-l. Zou, Z. Shen, and H. X. Tang, High quality factor surface Fabry-Perot cavity of acoustic waves, *Appl. Phys. Lett.* **112**, 073505 (2018).
- [17] K. Kokkonen and M. Kaivola, Scanning heterodyne laser interferometer for phase-sensitive absolute-amplitude measurements of surface vibrations. *Appl. Phys. Lett.* **92**, 063502 (2008).
- [18] Z. Shen, X. Han, C.-L. Zou, and H. X. Tang, Phase sensitive imaging of 10 GHz vibrations in an AlN microdisk resonator, *Rev. Sci. Instrum.* **88**, 123709 (2017).

- [19] R. Whatmore, P. Goddard, B. Tanner, and G. Clark, Direct imaging of travelling Rayleigh waves by stroboscopic X-ray topography. *Nature* **299**, 44 (1982).
- [20] E. Zolotoyabko, D. Shilo, W. Sauer, E. Pernot, and J. Baruchel, Visualization of 10 μm surface acoustic waves by stroboscopic x-ray topography. *Appl. Phys. Lett.* **73**, 2278 (1998).
- [21] D. Roshchupkin, T. Fournier, M. Brunel, O. Plotitsyna, and N. Sorokin, Scanning electron microscopy observation of excitation of the surface acoustic waves by the regular domain structures in the LiNbO_3 crystals. *Appl. Phys. Lett.* **60**, 2330 (1992).
- [22] D. Roshchupkin, M. Brunel, R. Tucoulou, E. Bigler, and N. Sorokin, Reflection of surface acoustic waves on domain walls in a LiNbO_3 crystal. *Appl. Phys. Lett.* **64**, 164 (1994).
- [23] L. Zheng, D. Wu, X. Wu, and K. Lai, Visualization of Surface-Acoustic-Wave Potential by Transmission-Mode Microwave Impedance Microscopy. *Phys. Rev. Applied* **9**, 061002 (2018).
- [24] L. Zheng, L. Shao, M. Loncar, and K. Lai, Imaging Acoustic Waves by Microwave Microscopy: Microwave Impedance Microscopy for Visualizing Gigahertz Acoustic Waves. *IEEE Microwave Magazine* **21**, 60 (2020).
- [25] D. Lee, Q. Liu, L. Zheng, X. Ma, H. Li, M. Li, and K. Lai, Direct Visualization of Gigahertz Acoustic Wave Propagation in Suspended Phononic Circuits. *Phys. Rev. Applied* **16**, 034047 (2021).
- [26] R. S. Weis and T. K. Gaylord, Lithium Niobate : Summary of Physical Properties and Crystal Structure. *Appl. Phys. A*, **37**, 191 – 203 (1985).
- [27] I. E. Kuznetsova, B. D. Zaitsev, A. A. Teplykh, S. G. Joshi, and A. S. Kuznetsova, The Power Flow Angle of Acoustic Waves in Thin Piezoelectric Plates. *IEEE Trans. Ultrason. Ferroelectr. Freq. Control*, **55**, 9 (2008).
- [28] R. Lu and S. Gong, Power Flow Angles of GHz Propagating Acoustic Waves in Thin -Film Lithium Niobate. To appear in *IEEE International Ultrasonic Symposium* (2021).
- [29] R. Lu, Y. Yang, and S. Gong, Acoustic Loss in Thin-Film Lithium Niobate: An Experimental Study. *IEEE Journal of Microelectromechanical Systems* **30**, 632 – 641 (2021).